



OPEN Investigation on the dynamic evolution and evaluation of floor microseismic responses during extra-thick coal seam mining

Haorui Wang^{1,2}✉, Shangxian Yin², Huiqing Lian², Min Cao²✉, Enke Hou¹, Xu Wang^{1,2} & Guofu Xing³

The mining of extremely thick coal seams causes strong disturbances to the floor strata. When a strong aquifer exists beneath the coal seam and the effective aquiclude is weak, the risk of floor water inrush increases significantly. In recent years, microseismic (MS) monitoring technology has been widely applied, and using MS monitoring to assess floor water inrush risk has proven to be a reliable and effective approach. To address the high-risk problem of floor water inrush during the extraction of extremely thick coal seams, this study employed MS monitoring to investigate the evolution characteristics of floor MS activity and its associated water inrush risk. The MS response characteristics induced by thick seam mining were analyzed, and a floor water inrush risk evaluation model was established based on the Analytic Hierarchy Process–Entropy Weight Method (AHP–EWM). The evaluation results were consistent with field monitoring data. The results indicate that most floor MS events in the 61607 working face of the Longwanggou Coal Mine were concentrated in the Taiyuan Formation. The MS monitoring indicators, such as the extent of the advanced influence zone, floor failure depth, and total daily released energy, showed strong correlations with observed data including water inflow and mine pressure. By summarizing the key controlling factors of floor water-inrush risk, this study departs from traditional static geological parameter indicators and instead focuses on dynamic indicators derived from the activity, spatiotemporal characteristics, and intensity characteristics of floor MS events. Integrating multiple influential factors of floor water inrush, a quantitative evaluation system for floor water-inrush hazard in extremely thick coal seam mining was established using the AHP–EWM combined subjective–objective weighting method, which shows good consistency with field monitoring results. This study provides theoretical and data support for analyzing the dynamic process and influencing factors of floor damage and fracture evolution under thick seam mining. It offers a new approach for predicting and forecasting water inrush risk, enriches the application of MS monitoring in mine floor water hazard prevention, and holds significant practical importance for promoting safe coal mine production.

Keywords Extra-thick coal seam, Floor failure, Microseismic monitoring, Risk evaluation

The coal resources in the Jin–Shan–Meng mining area of China are characterized by large reserves and thick coal seams¹. With the continuous progress of coal mining technology, a high-intensity and high-efficiency mining mode has been gradually established. Compared with conventional thin and medium-thick coal seams, the mining of extra-thick coal seams is associated with higher strata pressure, stronger ground stress effects, and greater disturbance to the floor, often resulting in extensive and deep floor fracturing^{2–6}. Moreover, the Carboniferous–Permian coal seam floors in China generally overlie Ordovician limestone aquifers with high water pressure. The fractures in the floor can easily connect with the aquifers and trigger water inrush disasters, posing serious threats to mine safety. Floor water hazards caused by high-pressure confined aquifers have become one of the main factors restricting the safe and efficient extraction of coal resources in China^{7,8}. Therefore, it is necessary to investigate the dynamic failure evolution of the floor during extra-thick coal seam mining.

¹College of Geology and Environment, Xi'an University of Science and Technology, Xi'an 710054, China.

²Hebei State Key Laboratory of Mine Disaster Prevention, North China Institute of Science and Technology, Beijing 101601, China. ³Inner Mongolia Zhongtai Suancang Mining Co., Ltd, Ordos 017000, China. ✉email: wanghr2333@163.com; caomin727@163.com

Many scholars have conducted studies on extra-thick coal seam mining and achieved valuable results. Zheng et al.⁹ analyzed the water inrush mechanism of the Huangyuchuan Mine during top-coal caving and clarified the coupling mechanism between Ordovician limestone permeable channels and floor failure, proposing a directional long-borehole exploration technique to prevent Ordovician limestone water hazards during mining. Shao¹⁰ systematically analyzed the roof and floor structure and failure characteristics of fully mechanized top-coal caving faces and established an elastic mechanical model of the floor. The study showed that the maximum failure depth of the floor is positively correlated with the face width and surrounding rock stress and negatively correlated with rock compressive strength. Li et al.¹¹ based on the gas–water two-phase flow similarity theory in fractured rock masses, established a CFDEM numerical model to simulate the fault-induced floor water inrush and roof–floor coupling failure in extra-thick coal seam mining. Their results indicated that the root cause of water inrush lies in the instability of key high-level strata, subsidence of masonry beams, and secondary fracturing of the floor. Wang et al.^{12–14} used theoretical analysis, numerical simulation, and field measurements to study the stress and fracture evolution of the floor during fully mechanized top-coal caving. Zhang et al.^{15–18} applied distributed optical fiber sensing and cross-hole resistivity CT testing to obtain in situ data on strain and geoelectric field responses during floor failure in extra-thick coal seam mining. Guo¹⁹ analyzed the three-dimensional dynamic evolution of floor disturbance using borehole stress–strain monitoring. Cao et al.²⁰ derived a mechanical relationship between floor failure depth and coal seam thickness and established a floor water inrush risk evaluation model using interval grey optimal clustering analysis.

In addition to floor failure research, Zhu et al.²¹ studied the mechanism of floor heave in fully mechanized top-coal caving faces and proposed an underground regional hydraulic fracturing technique for controlling floor heave. Zhang et al.^{22,23} investigated the characteristics of roof caving structure and dynamic loading mechanisms, analyzing the strong dynamic pressure phenomena in working faces of extra-thick seams. Kong et al.^{24,25} examined the evolution of fractures and seepage characteristics during mining and developed a predictive model for the height of the water-conducting fracture zone. Yu et al.²⁶ explored the multi-field coupling mechanism of disaster formation and proposed a collaborative control technology.

Most existing studies have been based on theoretical analysis, numerical simulation, and field measurements, which have limited continuity and fail to fully represent the dynamic evolution process of floor failure. As a real-time, dynamic, and efficient geophysical monitoring technique, MS observation has been increasingly applied in floor safety studies²⁷. Yin et al.²⁸ used machine learning and deep learning models to analyze MS events and successfully predicted water inrush incidents. Xin et al.²⁹ applied cumulative and kernel density indicators of MS events to interpret fault activation characteristics in the floor. Jia et al.^{30,31} established a water inrush risk evaluation method based on MS events, while Gai et al.^{32,33} introduced weighted variation coefficients and floor safety indices to improve the risk evaluation model and zoning accuracy. Xu et al.^{34,35} proposed an all-time–space early warning method for floor water inrush using MS monitoring, achieving accurate prediction at different mining stages. Zuo et al.^{36–38} combined theoretical analysis, MS monitoring, and numerical simulation to identify and predict potential water inrush channels based on floor rock fracture characteristics.

Although these studies have explored various aspects of floor water hazard prevention using MS technology and developed related theories and prediction methods, the understanding of floor failure characteristics and evaluation systems under special mining conditions remains incomplete. This is especially true for extra-thick coal seam mining in western China, where the large mining height produces strong and complex disturbances to the floor. Most hazard evaluations are based on static geological parameters such as aquiclude thickness, aquifer water pressure, and geological structures. The core logic relies on assessing the potential for water inrush from inherent geological conditions, but dynamic indicators are generally lacking. Therefore, taking the Longwanggou Coal Mine in the Zhungeer Coalfield as the research area, this study applies MS monitoring technology to analyze the dynamic evolution of floor failure. Based on the AHP-EWM method and combined with field water inrush data, a MS dynamic indicator system was established to evaluate floor water inrush risk, enabling real-time monitoring and quantitative assessment of the hazard. The research results can further enhance the application of MS technology in floor water hazard prevention and provide theoretical support for similar mining operations, offering practical significance for improving coal mine safety.

Study area overview

The Longwanggou Coal Mine is located in the central part of the Zhungeer Coalfield, Inner Mongolia, China. It belongs to the Dongsheng Subzone of the Ordos Stratigraphic Subregion within the North China Stratigraphic Region. The main mining seam is the Carboniferous Taiyuan Formation coal seam. The 61607 working face is situated in the northern wing of the 61 st panel district. The western side of the panel is bounded by intact coal and rock strata, while the eastern side is adjacent to the goaf area, as shown in Figure 1.

The working face has a strike length of 1,276.2 m, an inclined length of 255 m, an average mining thickness of 21.6 m, and a burial depth ranging from 280.4 to 426.8 m, with an average dip angle of 3°. The lithological profile of the roof and floor strata of the 61607 working face is shown in Figure 2. The main aquifer in the floor is the karst fissure aquifer of the Ordovician limestone. The principal water-bearing section is the Middle Ordovician Majiagou Formation, whose upper part consists of light gray argillaceous limestone and thick-bedded limestone interbedded with thin layers of gray limestone. The lower part is composed of dolomitic limestone and thick-bedded dolomite, with well-developed dissolution fissures, cavities, and pores. The unit water inflow varies between 0.024 and 34.321 L/s·m, indicating weak to extremely strong water richness.

The distance between the floor of the working face and the top boundary of the Ordovician limestone ranges from 33 to 53.3 m, with an average of 44.57 m. The Bauxite-bearing mudstone of the Carboniferous Benxi Formation, with an average thickness of about 8.22 m, serves as an effective aquiclude between the coal seam floor and the Ordovician aquifer.

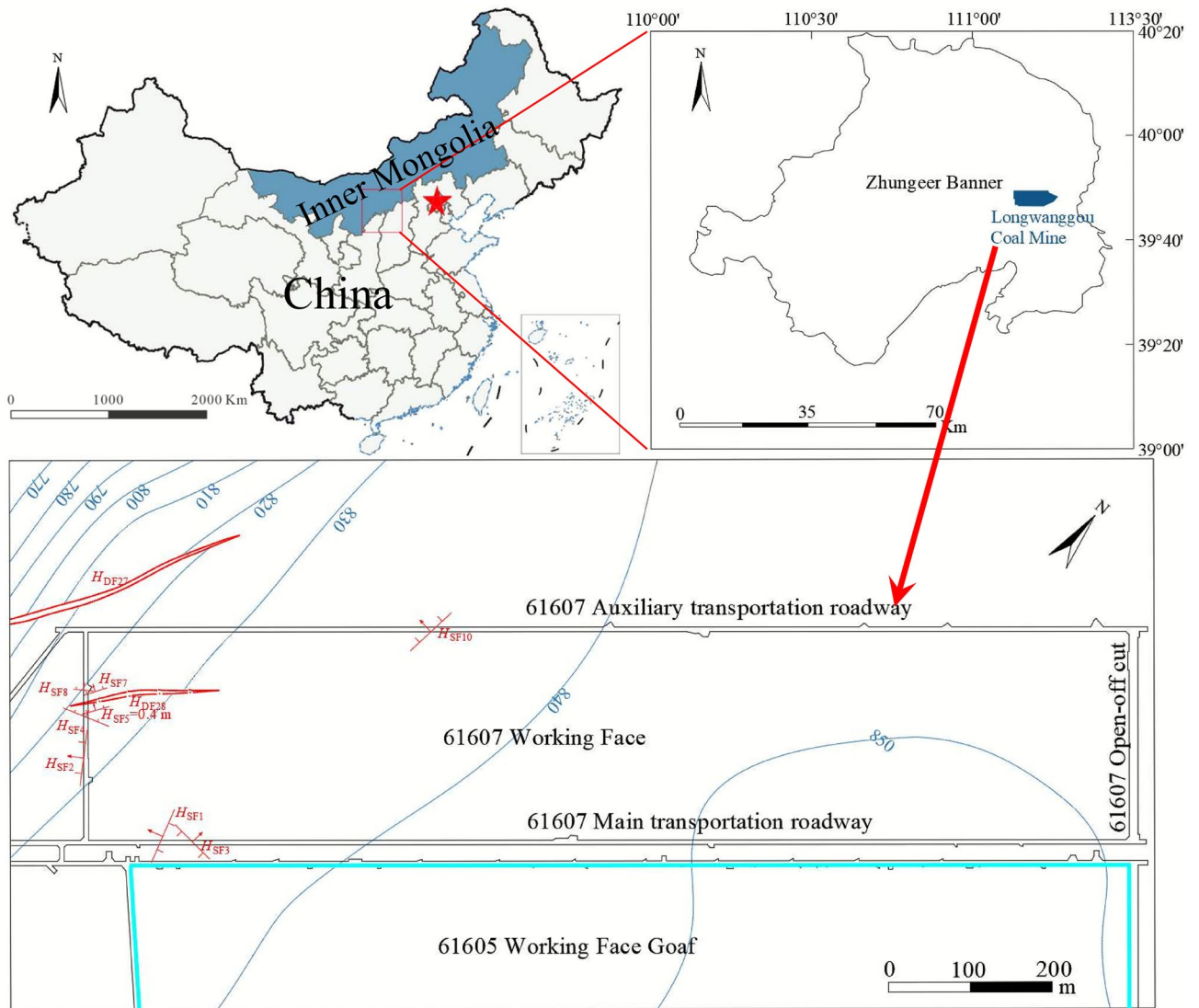


Fig. 1. Working Face 61607, Longwanggou Coal Mine, Inner Mongolia, China.

Research methods

Microseismic monitoring system

The 61607 working face of the Longwanggou Coal Mine is monitored using the KJ551 underground MS monitoring system^{27,39–42}. The system structure is shown in Figure 3. MS sensors installed in the survey area receive vibration signals, which are transmitted to the MS monitoring substation. Signals are then sent through a ring network to the data acquisition host and subsequently to the data storage and processing host. The processing host performs secondary filtering, noise reduction, events localization, and multi-directional visualization of MS events.

The KJ551 MS system employs high-sensitivity sensors (100 V/m/s) with a wide frequency range (0.1–600 Hz). For signal transmission, an advanced combination of cable and optical fiber technology is used. Cable transmission can cover distances of at least 10 km, while optical fiber transmission can reach up to 60 km, meeting the requirements of large-scale mining operations.

Based on the actual conditions of the 61607 working face, two MS substations were deployed, each installed in a well-conditioned chamber. The boreholes were drilled to a vertical depth of approximately 2.4 m, and the geophones were anchored along the full length using $\phi 22$ mm cement bolts with resin adhesive at the bottom. A cement pad was placed at the borehole mouth, leaving the bolt exposed by 0.05–0.1 m. The geophones were connected to the ends of the bolts using universal joints. Except for the first sensor, which was located 50 m from the cut-through, the spacing between adjacent sensors was approximately 100 m. After installation, each sensor underwent on-site hammer testing to ensure signal quality.

Once the substations and sensors were installed, calibration blasting tests were conducted in the two main entries of the working face to ensure precise sensor positioning. The elastic wave velocity of the surrounding rock was accurately determined based on the blasting signals received by the sensors, allowing the calculation of

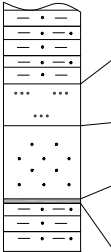

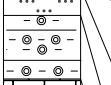
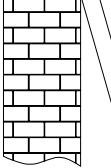
Stratum	Bar Chart	Lithology	Thickness/m	Description
P _{1s}		sandy mudstone	11.30	Gray to dark gray, blocky, silty and muddy texture
		fine sandstone	5.42	Gray white, thick layered, fine-grained sandy structure
		coarse sandstone	7.27	Gray white, blocky, coarse-grained sandy structure
		No.5 coal seam	0.61	Black, with a multi-layered structure and multiple interlayers of mudstone
C _{2t}		sandy mudstone	6.22	Dark gray, with a muddy texture
		coarse sandstone	13.21	Gray white, blocky, coarse-grained sandy structure
		mudstone	11.35	Dark gray, mudstone structure, blocky
		No.6 coal seam	21.60	Black, striped brown, containing 5-14 layers of dirt bands
		mudstone	4.72	Dark gray, mudstone structure, soft texture, blocky
		fine sandstone	6.40	Gray white, fine-grained structure, argillaceous cementation, hard
		mudstone	5.31	Gray black, with a muddy structure and a small amount of coal seam
		middle sandstone	3.79	Gray white, medium (fine) grain structure, relatively hard
		mudstone	5.02	Reddish brown, mudstone structure, containing feldspar, soft texture
		siltstone	5.40	Gray white, mainly composed of quartz and feldspar, relatively hard
C _{2b}		mudstone	3.50	Gray black, with a muddy structure, dense, and relatively soft
O ₂		fine sandstone	3.51	Gray white, medium (fine) grain structure, relatively hard
		bauxitic mudstone	8.22	Yellow green, muddy structure, smooth fracture surface
		limestone	> 230	Gray white, light gray, Baiyun limestone, mud-limestone

Fig. 2. Comprehensive stratigraphic column of roof and floor at working face 61607.

the actual average wave velocity of the rock mass. Using this wave velocity, the source location of the test blasts was analyzed to validate the system's positioning accuracy.

The obtained velocity model and the actual sensor positions were imported into the processing software. During actual mining operations, the time differences of arrival at each MS sensor were used to calculate the source location and energy of events. This enabled determination of the spatial-temporal characteristics and energy levels of each MS events, providing the basis for corresponding early-warning measures.

Analytic hierarchy process-entropy weight method (AHP-EWM)

Analytic hierarchy process

The Analytic Hierarchy Process⁴³⁻⁴⁵ (AHP) is a method for calculating weights both qualitatively and quantitatively. It involves three main steps:

- (1) Constructing a hierarchical structure model: The decision problem is decomposed into a hierarchical structure of goal layer-criteria layer-indicator layer.
- (2) Building the judgment matrix: For elements at the same hierarchical level, a relative importance scale is used. Experts are invited to score the importance of each element, forming a judgment matrix $A=(a_{ij}) n \times n$, where n is the number of elements at that level. The matrix satisfies reciprocity and reflexivity.
- (3) Weight calculation and consistency test: The maximum eigenvalue λ_{max} and its corresponding eigenvector ω of matrix A are determined. The weights ω_{AHPj} for each element are calculated accordingly. The consist-

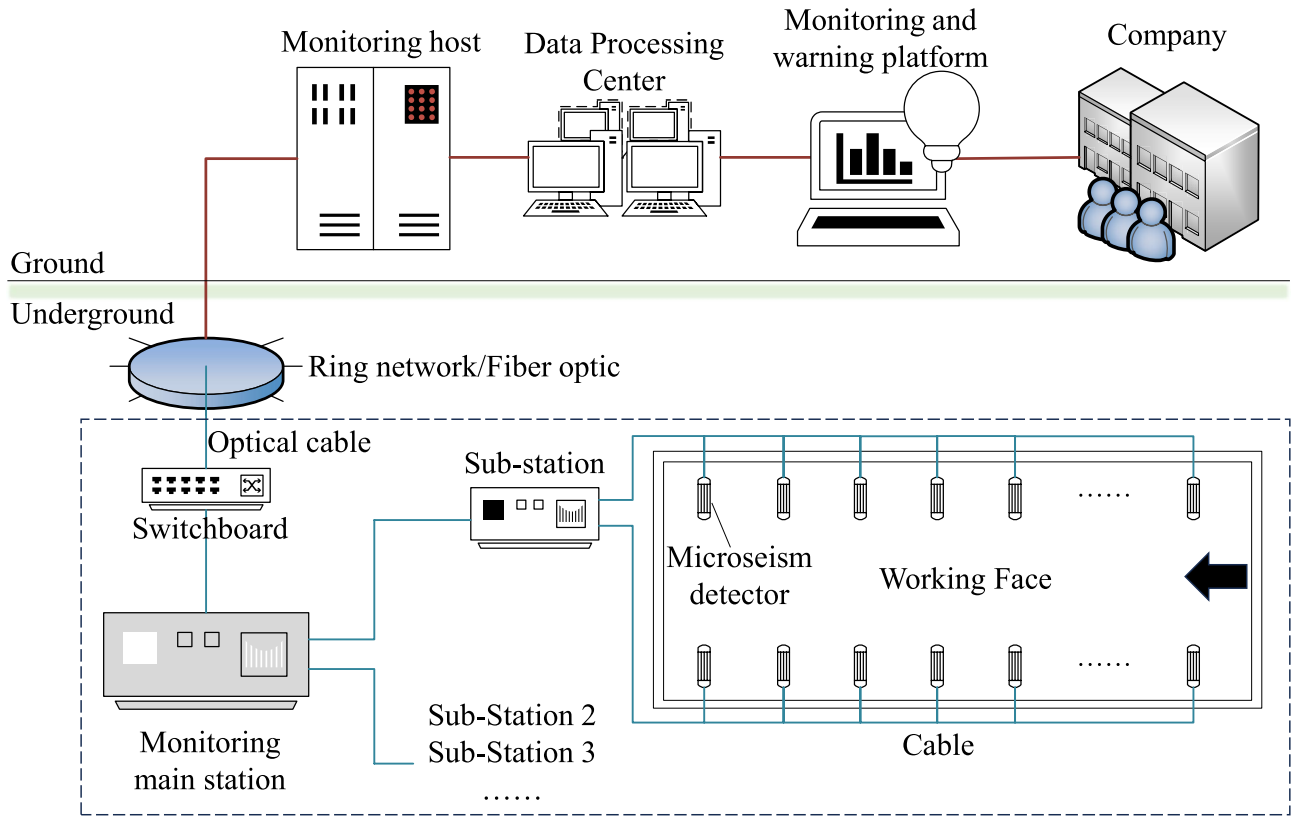


Fig. 3. Schematic diagram of the MS monitoring system.

ency index (CI) and consistency ratio (CR) are computed to ensure $CR < 0.1$, avoiding logical contradictions in the judgments. The formulas are:

$$CI = \frac{\lambda_{max} - r}{r - 1} \quad (r > 1) \tag{1}$$

$$CR = \frac{CI}{RI} \tag{2}$$

where CI is the consistency index, λ_{max} is the maximum eigenvalue of the judgment matrix, r is the matrix order, and RI is the random consistency index.

Entropy weight method

The Entropy Weight Method^{46,47} (EWM) is based on information entropy theory. It quantifies the contribution of each indicator to the decision-making process according to its data dispersion, achieving objective weighting. The steps are as follows:

- (1) Data normalization: Since the indicators differ in dimension and magnitude, the raw data are normalized.
- (2) Calculation of information entropy: For the i -th sample of the j -th indicator, the probability p_{ij} is calculated. The entropy value E_j of each indicator is then obtained using the information entropy formula.
- (3) Determination of indicator weights: Smaller entropy E_j indicates larger data dispersion and more effective information. The weight of the j -th indicator is calculated as:

$$p_{ij} = \frac{x_{ij}}{\sum_{i=1}^m x_{ij}} \tag{3}$$

$$E_j = -\frac{1}{\ln m} \sum_{i=1}^m p_{ij} \ln p_{ij} \tag{4}$$

$$\omega_{EWM,j} = \frac{1 - E_j}{\sum_{i=1}^n (1 - E_j)} \tag{5}$$

where x_{ij} is the normalized value of the j -th indicator for the i -th sample, m is the number of samples, n is the number of indicators, and $1 - E_j$ represents the information utility.

Vulnerability index method

The Vulnerability Index Method is a mature evaluation model commonly used for floor water inrush risk assessment^{48–52}. The vulnerability index I is calculated as:

$$I = \sum_{j=1}^n \omega_j \cdot x_{ij} \quad (6)$$

Combining AHP and EWM, the composite weight ω_j is calculated as:

$$\omega_j = \frac{\omega_{AHP,j} \cdot \omega_{EWM,j}}{\sum_{j=1}^n \omega_{AHP,j} \cdot \omega_{EWM,j}} \quad (7)$$

where ω_j is the weight of the j -th indicator, ω_{AHPj} and ω_{EWMj} are the weights obtained from AHP and EWM, respectively, and n is the number of evaluation indicators.

Results

Overview of microseismic monitoring

The study period was from April 1, 2023, to August 31, 2023, during which the 61607 working face advanced a total of 416.7 m, with an average daily advance of approximately 4 m. Based on the comprehensive geological column of the 61607 working face and actual mining exposure, the recorded MS events were classified according to the stratigraphic layers. The frequency of MS events for each layer is summarized in Table 1.

Before mining, hydraulic pre-fracturing was applied to the roof, causing partial roof failure. The compromised roof integrity interrupted the stress transmission paths, resulting in a relatively small number of roof MS events, accounting for only 4.33% of the total events. Therefore, this study focuses on floor failure, and roof-related events are not further discussed.

Statistical analysis shows that MS events in the floor accounted for 92.92% of all recorded events within the study interval. This indicates that the closer the rock mass is to the coal seam floor, the more significant the disturbance under mining-induced stress, making it more susceptible to failure and stress-concentration fracturing.

The Carboniferous Benxi Formation and Ordovician Formation accounted for 1.73% and 1.02%, respectively. Although floor failure is mainly concentrated in the Taiyuan Formation, in areas with concealed structures, local floor disturbance can extend deeper, breaking through the Benxi Formation aquiclude and reaching the Ordovician aquifer. According to MS monitoring, the deepest disturbed point in the floor was 83.55 m below the coal seam floor, reaching the Ordovician limestone strata.

To more intuitively illustrate the temporal variation of MS events, daily frequency histograms for roof and floor MS events and a daily average advance length line chart were plotted, as shown in Figure 4. The frequency of MS events showed distinct peaks on April 22, July 15, and August 4, and overall increased after August 16. Further analysis indicates that these abnormal increases were not only closely related to the advancement rate but also influenced by the stage-wise variations in overlying strata structure and floor stress conditions. Around April 22, a sudden change in overlying strata stress rapidly activated floor joints under concentrated compressive-shear action, resulting in the first MS peak. In mid-July, the overlying strata transitioned from initial to periodic stress, causing staged fracture in key layers and transient stress release, which led to the second peak. On August 4, the working face passed critical locations with underlying hard rock layers or intact limestone sections, and floor joints at depth were reopened⁵³ under the combined effect of water pressure and concentrated stress, producing the third peak. After August 16, the face entered the “secondary caving” stage, where the expanded mining space, superimposed advance support pressure, and secondary subsidence of overlying strata maintained the floor in a high-disturbance state, resulting in an overall increase in MS event frequency.

Spatiotemporal response characteristics of floor microseismic events

Floor MS events represent energy-releasing fractures in the floor rock and can directly reflect the degree of floor failure across different strata in both space and time. In the 61607 working face, the floor aquiclude is relatively thin. The propagation of primary fractures or the development of concealed structures can easily connect to the floor aquifer, increasing water inflow or even causing water inrush. To better understand the impact of mining on floor disturbance, the spatiotemporal distribution characteristics of floor MS events were analyzed from the perspectives of time, space, and energy.

	Layer	Frequency	Percentage/%	Cumulative percentage/%
Roof	Above the roof	280	4.33	4.33
Floor	Carboniferous Taiyuan Formation	6008	92.92	97.25
	Carboniferous Benxi Formation	112	1.73	98.98
	Ordovician	48	1.02	100

Table 1. Frequency statistics of MS events at working face 61607 (Apr 1–Aug 31, 2023).

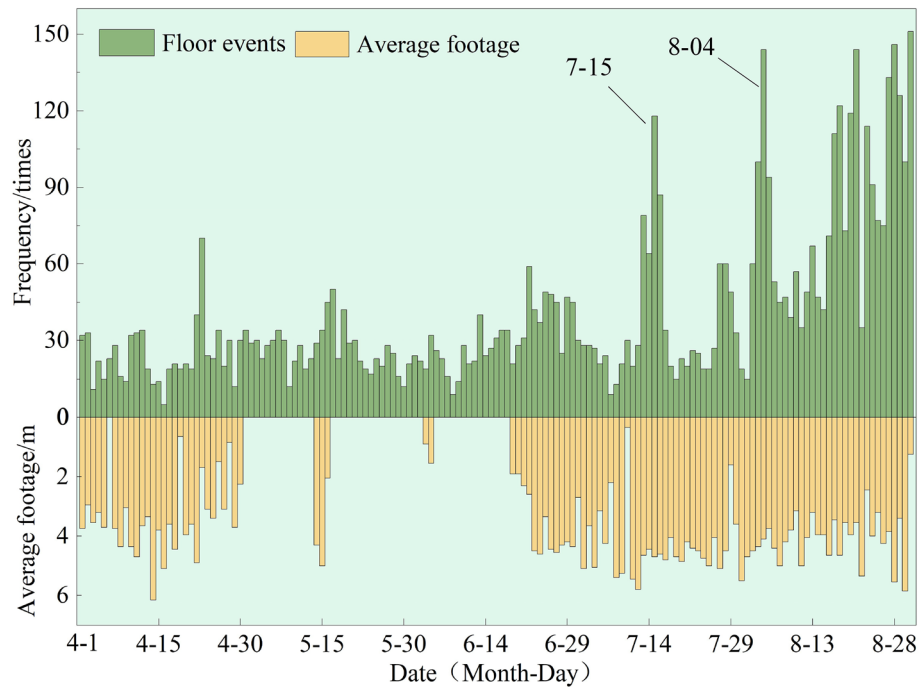


Fig. 4. Frequency statistics of MS events at working face 61607 (Apr 1–Aug 31, 2023).

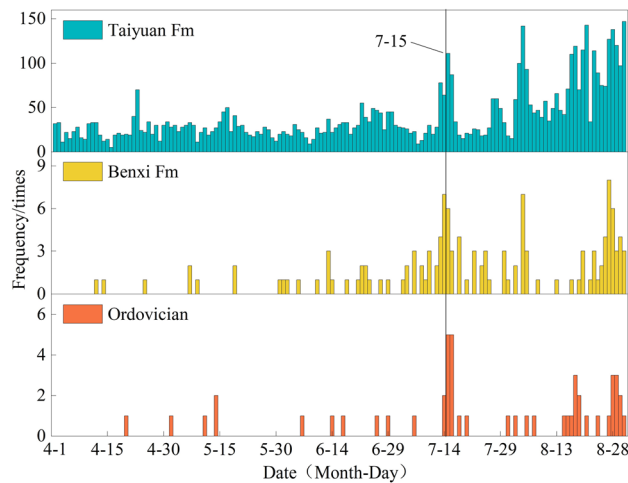


Fig. 5. Histogram of MS events frequency in different floor strata.

Temporal distribution characteristics

The Carboniferous Benxi Formation lies below the floor failure zone and above the Ordovician limestone aquifer. This aquiclude mainly consists of bauxite-bearing mudstone and mudstone, with the bauxite-bearing mudstone layers being thick, lithologically stable, and possessing high uniaxial compressive strength, making it an effective floor aquiclude. If this layer is compromised, the integrity of the floor aquiclude may be lost, forming a water-conducting channel through which pressurized water can rise along fractures, potentially causing water inrush. Therefore, the Benxi Formation can be treated as a monitoring alert layer in MS studies.

Daily floor MS events frequencies were counted for each stratigraphic layer and plotted (Figure 5). From April to June, MS events frequency remained relatively stable, with low frequencies in both the Benxi Formation and Ordovician strata. On July 15, MS events increased noticeably, particularly in the Benxi alert layer and the Ordovician aquifer, indicating intensified disturbance. After August 4 and 16, floor MS events frequencies continued to rise synchronously, reflecting further destabilization of the Ordovician limestone aquifer.

Comparison with real-time monitoring of water inflow and Ordovician limestone water levels (Figure 6) shows two significant water level drops during the study period. The first occurred from April 30 to May 10, without a corresponding increase in inflow. MS events frequencies in the Benxi alert layer and Ordovician

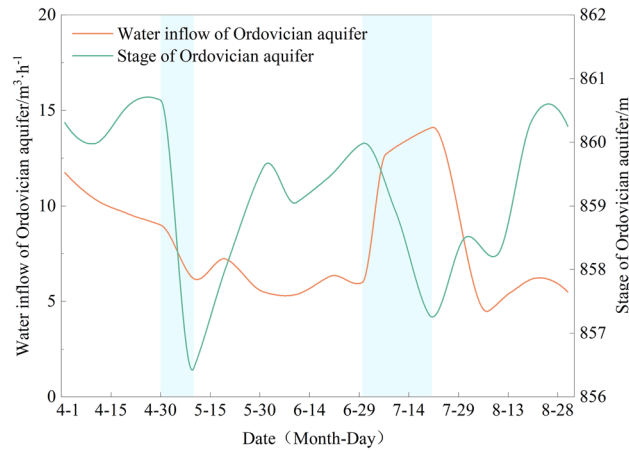


Fig. 6. Variation trend of water inflow and ordovician limestone water level in the working face.

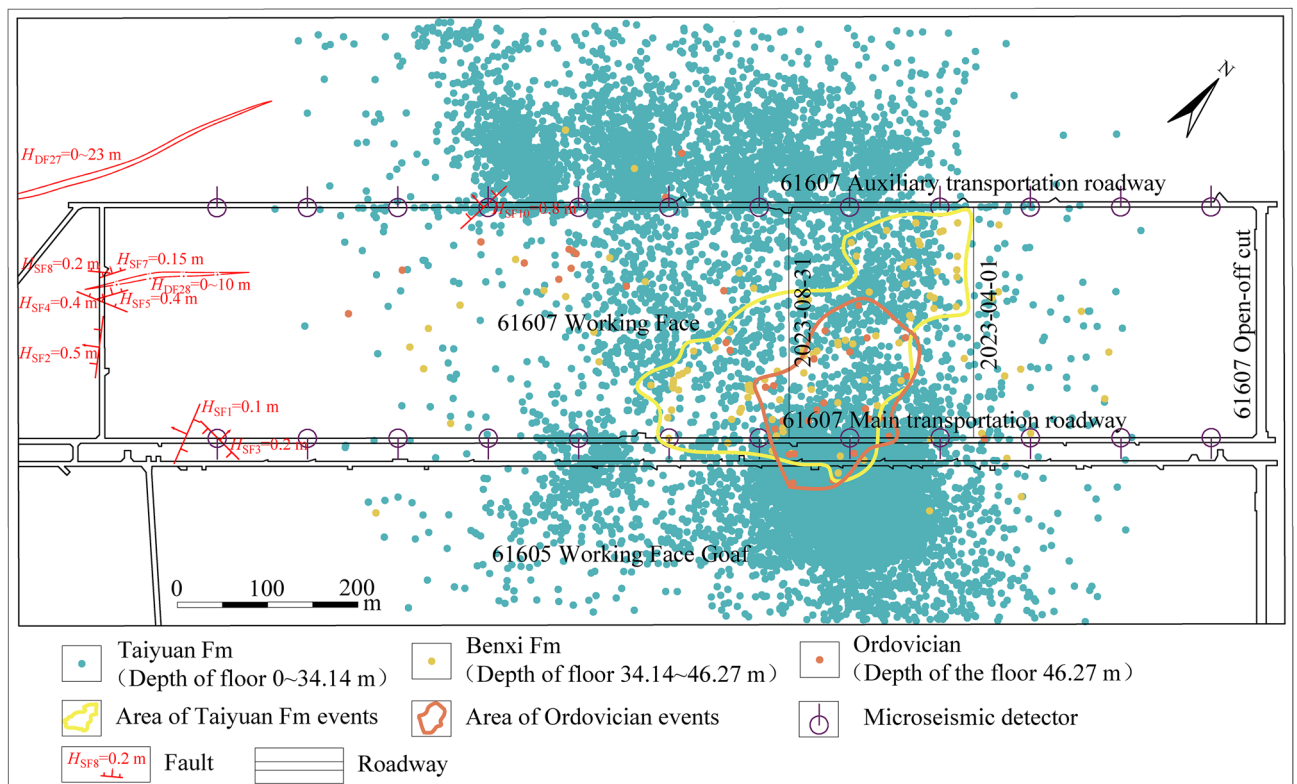


Fig. 7. Plan distribution map of floor MS events.

strata remained low, suggesting that floor failure was confined to the Taiyuan Formation and had not yet connected to the Ordovician aquifer. The second drop occurred from June 30 to July 20, during which water inflow increased significantly between June 30 and July 31. From July 15, MS events frequency in the Benxi alert layer and Ordovician strata rose sharply, indicating that floor failure had developed into the Benxi Formation and the top of the Ordovician aquifer. Consequently, water inflow increased markedly, demonstrating a strong hydraulic connection between floor fractures and the aquifer. However, no water inrush occurred, suggesting that although mining-induced fractures communicated with the aquifer, some fractures were reclosed under high-stress conditions due to the large mining height, limiting water-conducting capacity.

Planar distribution characteristics

The planar distribution of floor MS events within the 61607 working face study area is shown in Figure 7. Events are primarily concentrated 640 m ahead of the mining face, with an outward extension of approximately 200 m along both roadway sides.

Examining the planar distribution of MS events by stratigraphic layer, the Taiyuan Formation exhibits the widest distribution. Events cluster near the SF10 fault and adjacent 61605 working face goaf, with concentration along the roadway sides significantly higher than in the center. This indicates that the post-mining surrounding rock experiences substantial vertical stress, leading to severe plastic deformation and release of potential energy. The clustering of MS events near the SF10 fault suggests that geologically weak zones are more susceptible to disturbance and failure.

MS events in the Benxi Formation and Taiyuan Formation are mainly concentrated in the central part of the working face. The distribution of MS events in the Benxi Formation is broader than that in the Ordovician strata. During the early stage of mining, MS events clustering in both layers was low, gradually increasing toward the mid-section around mid-July. Combined with water inflow and Ordovician water level data (Figure 6 and Figure 7), the increase in MS events frequency in the Benxi alert layer corresponds with a drop in Ordovician water level and an increase in water inflow, lasting until the end of July. After the mining face passes through this region, the Ordovician water level rises while water inflow decreases.

The MS events clusters in the Benxi and Ordovician strata form irregular elliptical patterns. This is attributed to roof pressure relief after mining, which causes the main stress to concentrate in the sidewalls. Consequently, lateral shear stress is imposed on the floor beneath the goaf, resulting in floor compression and expansion toward the goaf. This lateral stress concentration in the central part of the working face leads to floor disturbance and fracturing.

Overall, the advance influence range of floor MS events in thick coal seam mining can reach up to 500 m, significantly exceeding the advance influence range of conventional thickness coal seams (200–300 m). This range is closely related to hydrogeological conditions and other factors. To investigate the dynamic evolution of the floor MS influence range, the daily MS events located ahead of the mining line are defined as the advance influence zone, while those located behind the mining line are defined as the rear influence zone, as illustrated in Figure 8. Daily distances of MS events in the advance and rear influence zones were statistically analyzed and plotted in a bar chart (Figure 9).

From April 1 to August 31, the advance influence distance continuously expanded with mining progress. During the early mining stage (April), the advance influence distance was relatively short, mostly within 200 m, indicating that early mining-induced stress had limited effect on floor disturbance. In the mid-mining stage (May–June), the advance influence distance extended to 300–400 m, and during the late mining stage (July–August), it reached a maximum of approximately 500 m. This indicates that the large mining height and strong disturbance of thick coal seam mining result in an advance influence range far exceeding that of conventional seams, a characteristic that becomes more pronounced as mining progresses.

In contrast, the rear influence distance remained smaller and relatively stable, generally within 200 m, suggesting that after stress release in the goaf, the continued disturbance on the floor is weak. Therefore, MS events are primarily dominated by stress concentration in the advance zone.

Vertical distribution characteristics

Based on the actual geological profile of the working face (along the main haulage entry), the vertical distribution of floor MS events was plotted as shown in Figure 10.

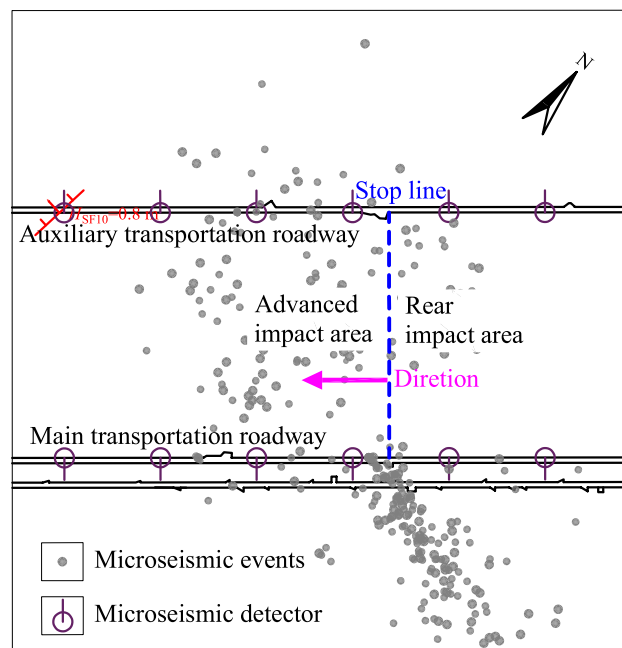


Fig. 8. Schematic diagram of the planar influence range of MS events.

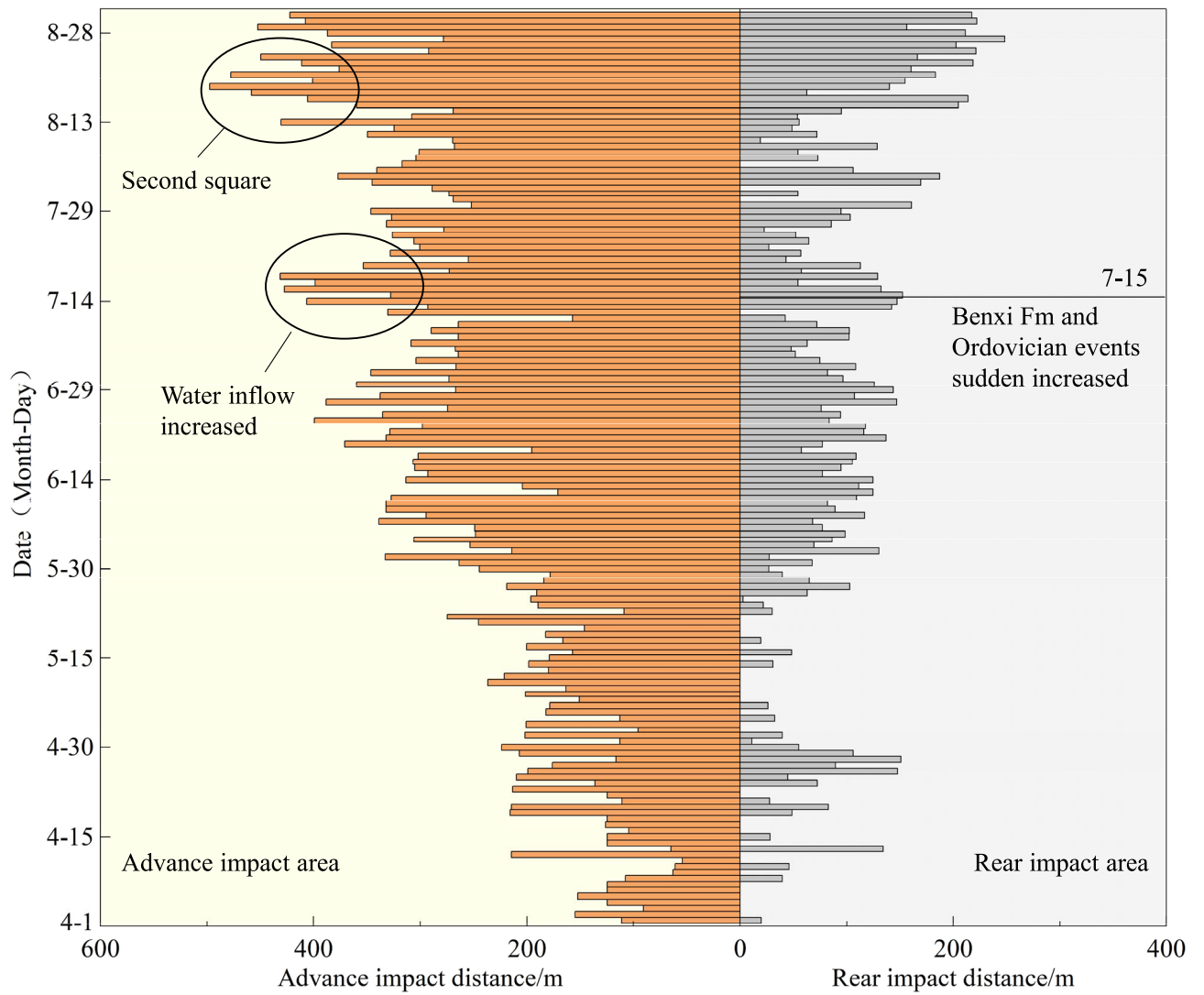


Fig. 9. influence distance before and after the mining line.

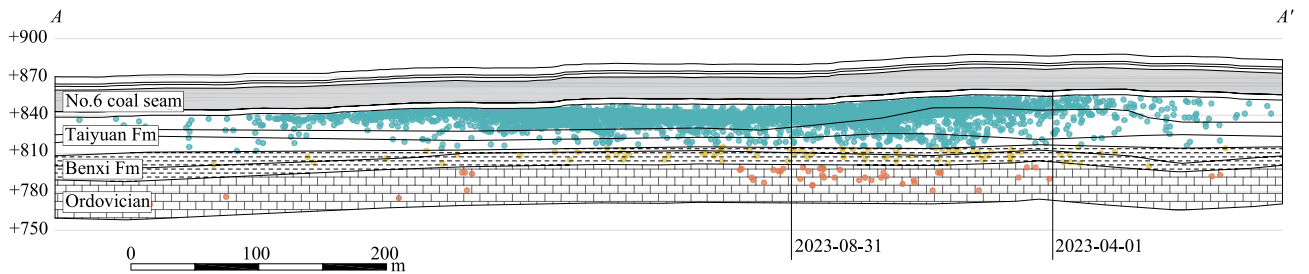


Fig. 10. Longitudinal section distribution of MS events along the roadway.

The Carboniferous Taiyuan Formation (colored in blue) exhibits the highest number and widest distribution of MS events, representing the primary layer of floor MS activity. The large mining height and associated stress from thick coal seam extraction directly act on this layer, causing frequent rock fracturing and the strongest MS responses.

In the Carboniferous Benxi Formation (yellow), MS events are significantly reduced and distributed sparsely beneath the Taiyuan Formation. The vertical transmission of mining-induced stress to this layer is weaker than in the Taiyuan Formation, resulting in a lower frequency of rock fracturing.

The Ordovician Formation (red) exhibits the fewest MS events, which are sporadic and scattered. The high rock strength and greater distance from the coal seam floor, coupled with the influence of mining-induced stress and floor water pressure, make this layer less susceptible to large-scale fracturing.

The development depth of floor MS events reflects the concentrated floor failure range and serves as a key indicator for floor water inrush early warning. By statistically analyzing the spatial coordinates of MS events, the spatial influence range, i.e., the development depth of floor MS events, can be determined. The development depth was segmented into 2 m intervals, and the corresponding MS events frequency, proportion, and cumulative proportion were calculated (Figure 11), providing a clear visualization of the vertical distribution of MS events.

MS events are highly concentrated in the shallow region beneath the coal seam floor, with the 0–28 m depth interval exhibiting peak frequency, accounting for approximately 96% of total events. This interval is directly below the coal seam floor and is subjected to mining-induced stress, resulting in rock failure primarily through tensile fracturing and shear slip, which represents the core zone of mining energy release and the strongest MS responses.

With increasing depth, MS events frequency decays exponentially. The 26–28 m interval accounts for about 0.59%, and the 28–30 m interval accounts for only 0.31%, indicating very few MS events beyond 28 m. Therefore, the concentrated floor failure zone based on MS monitoring is considered to extend up to 28 m below the coal seam floor.

According to the ‘Code for Design on Pillar Reserving and Pressure Coal Mining of Buildings, Water Bodies, Railways, and Major Tunnels,’ a large number of observed values of floor damage depth are statistically analyzed. Using the linear regression method, factors influencing the depth of floor damage, such as the inclined length of the working face, coal seam mining depth, coal seam mining thickness, and working face inclination angle, are taken into consideration. The mining-induced floor failure depth h can be estimated using the empirical formula:

$$h = 0.0085H + 0.1665\alpha + 0.1079L - 4.3579 \tag{8}$$

where L is the working face dip length (m), α is the coal seam dip angle ($^\circ$), and H is the mining depth (m). For the 61607 working face, $L=255$ m, $\alpha=3^\circ$, and H is taken as the average burial depth of 353.6 m. Substituting these values yields a floor failure depth of 26.66 m.

The MS monitoring analysis results show a maximum deviation of less than 5% from the theoretical empirical calculation, indicating that the floor failure depth derived from MS monitoring is reasonable and reliable.

Energy distribution characteristics

The energy of MS events quantitatively represents the release of elastic potential energy during rock fracturing, and can effectively reflect the scale, intensity, and degree of mining-induced stress disturbance in the rock mass. To further investigate the intrinsic relationship between MS events energy and mining-induced stress manifestation, the daily cumulative energy of floor MS events was analyzed in conjunction with the maximum subsidence of hydraulic support columns in the roadway, as shown in Figure 12.

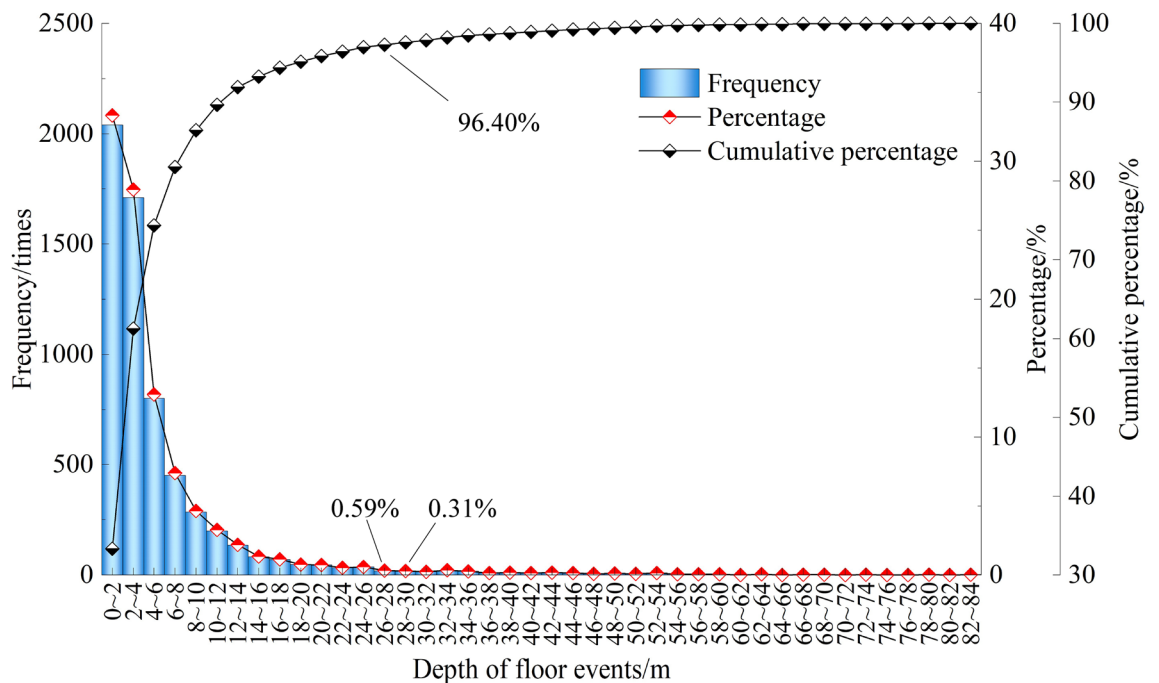


Fig. 11. Statistical chart of floor MS events development depth.

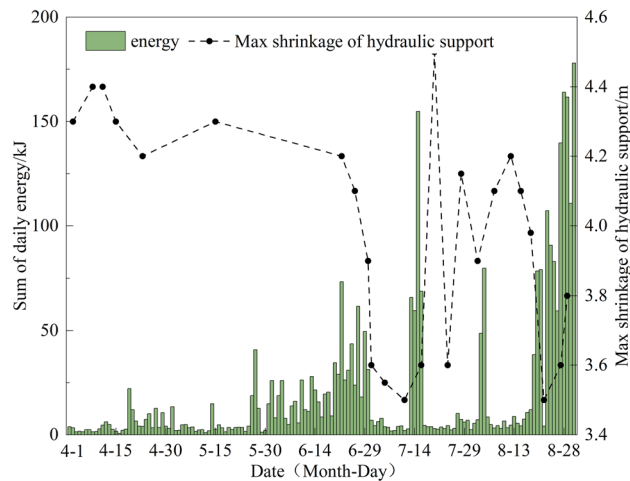


Fig. 12. Daily total energy of floor MS events and variation of maximum hydraulic support convergence.

The daily cumulative MS energy exhibits an overall “low–high–low–high” trend. During the early and mid-mining stages (April–June), daily cumulative energy remained at a relatively low level with small fluctuations. During this period, the working face was in the “initial stress adjustment” stage, and mining-induced disturbances to the floor were relatively mild. Rock fracturing was limited in scale and frequency, the maximum subsidence of hydraulic supports was stable, mining-induced stress on the floor was low, and water inflow remained stable without significant increase.

In the late mining stage (July–August), daily cumulative energy experienced a sudden surge around mid-July, coinciding with a corresponding increase in maximum hydraulic support subsidence. This period was accompanied by strong manifestation of mining-induced stress, a drop in limestone water level, and an increase in water inflow, indicating that as mining progressed, stress accumulation and release in the floor entered a high-disturbance stage. Large-scale, high-energy rock fracturing occurred, and MS responses intensified significantly. In late August, as the working face entered the “secondary square” stage, both daily cumulative energy and mining-induced stress increased again.

The spatial distribution of MS events energy in the Carboniferous Benxi Formation and deeper strata from June to August is shown in Figure 13. In June, MS events were sparse and scattered, indicating weak disturbance of the Benxi Formation and deeper layers by mining-induced stress. In July, MS events frequency increased significantly, with the occurrence of multiple high-energy events, although clustering remained low. During this stage, mining-induced stress propagated from the coal seam floor to the overlying strata, markedly enhancing floor disturbance; both the frequency and scale of rock fracturing increased, and energy release intensified. In August, high-energy MS events became concentrated, forming strip-like distributions along the working face near the main haulage entry. The Benxi Formation and deeper strata experienced large-scale, concentrated rock fracturing, leading to the development and connectivity of floor fractures, and stress accumulation and release reached a peak.

The temporal evolution of floor MS energy exhibits a characteristic pattern of “early low-energy stability, late high-energy burst”, which is closely coupled with mining-induced stress manifestation and water inflow changes. High-energy MS events are the key factor driving the extension of floor failure to greater depths and provide a direct basis for establishing energy-threshold-based early warning for floor water inrush risk.

Floor water inrush hazard evaluation based on AHP-EWM

Indicators for floor water inrush hazard

Based on the spatiotemporal characteristics of floor MS events analyzed in Section “[Spatiotemporal response characteristics of floor microseismic events](#)”, the MS-based indicators directly reflecting the floor water inrush hazard can be classified into three categories: activity indicators, spatiotemporal indicators, and intensity indicators.

(1) Activity Indicators. As discussed in section “[Temporal distribution characteristics](#)”, the activity of floor MS events reflects the degree of rock fracturing and floor disturbance. The selected activity indicators include: Daily frequency of floor MS events and daily frequency of MS events in the Benxi Formation and deeper strata.

(2) Spatiotemporal Indicators. The formation of water-conducting channels is a necessary but not sufficient condition for water inrush. The spatiotemporal distribution of MS events can reflect the development and connectivity of these channels. Therefore, the selected spatiotemporal indicators include: Maximum daily development depth of floor MS events and advance influence distance of MS events.

The Benxi Formation serves as a key floor aquiclude, and when the maximum daily development depth of floor MS events exceeds the Benxi Formation, it indicates an increased risk of water inflow, potentially leading to enhanced water discharge or even floor water inrush. The dynamic trend of this indicator can be directly linked to the evolution of mining-induced water-conducting fracture channels.

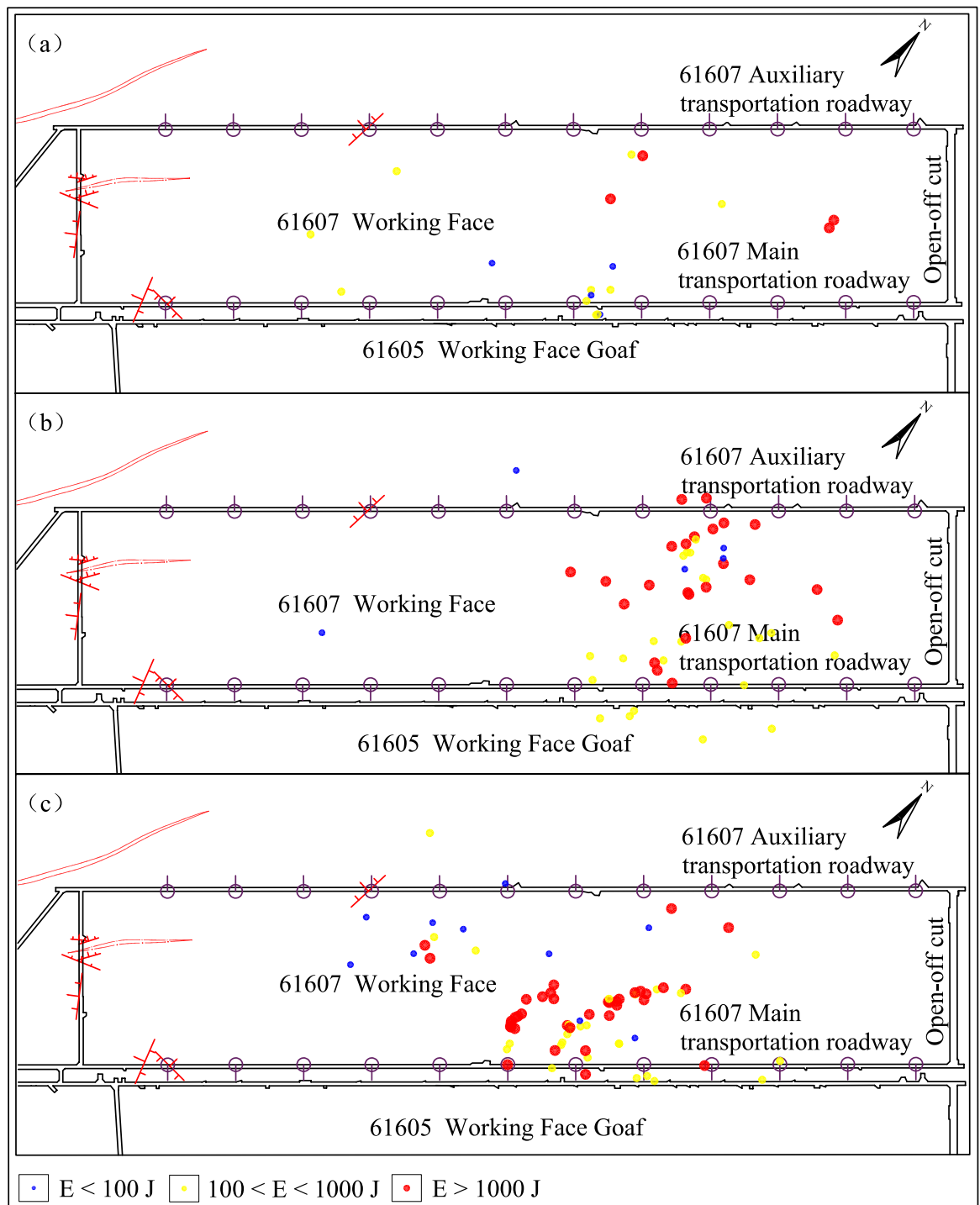


Fig. 13. Energy distribution of ms events in the benxi formation and deeper strata: (a) June; (b) July; (c) August.

The maximum daily development depth of floor MS events was plotted as a point-line graph (Figure 14) to analyze the dynamic relationship between water inflow and floor failure depth during the mining of the 61607 working face. As shown in Figure 14, after July 14, the daily maximum floor failure depth increased, reaching the Ordovician strata. In geologically weak zones or areas with pre-existing fractures, thick coal seam mining can cause more intense floor damage, increasing the likelihood of new water-conducting fractures or enhanced water inflow.

(3) Intensity Indicators. As analyzed in Section "Energy Distribution Characteristics", the energy of floor MS events reflects high-energy, large-scale fracturing and its impact on mining-induced stress manifestation, illustrating that MS events energy is closely associated with mining stress and the development of water-

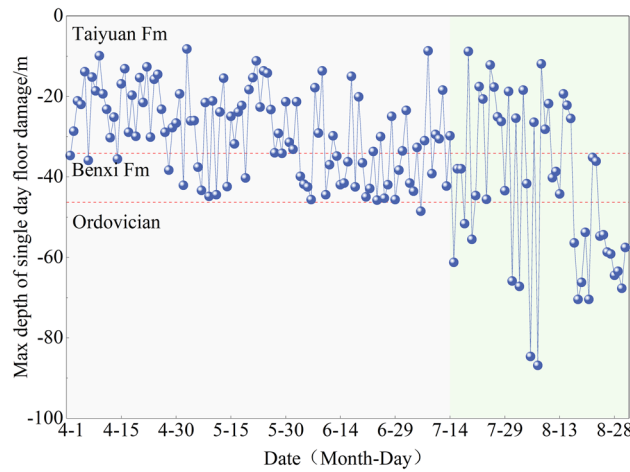


Fig. 14. Point-line chart of the daily maximum development depth of floor MS events.

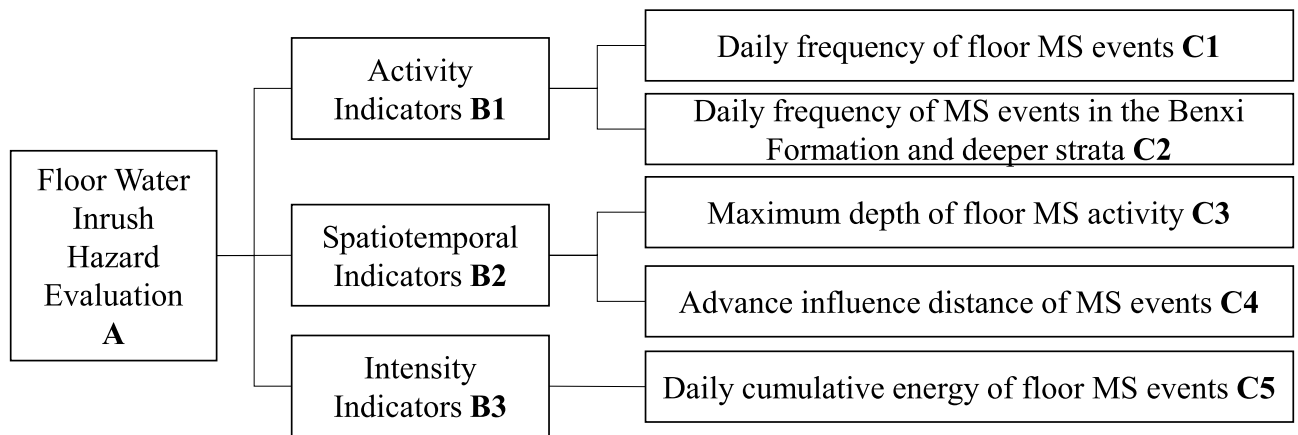


Fig. 15. The evaluation indicator system.

Indicators	B1	B2	B3
B1	1	1.15	3.90
B2	1/1.15	1	3.38
B3	1/3.90	1/3.38	1

Table 2. Judgment matrix for first-level indicators.

conducting channels. Therefore, the daily cumulative energy of floor MS events is selected as the intensity indicator.

Based on the above analysis, five MS events indicators were identified to evaluate the floor water inrush hazard, reflecting the activity, spatiotemporal, and intensity characteristics of floor MS events: daily frequency of floor MS events, daily frequency of MS events in the Benxi Formation and deeper strata, maximum daily development depth of floor MS events, advance influence distance of MS events, and daily cumulative energy of floor MS events.

The evaluation indicator system is shown in Figure 15. All five indicators exhibit a positive correlation with the floor water inrush hazard, i.e., higher values correspond to higher risk.

Weight calculation of floor water inrush hazard indicators

The weights of the floor water inrush hazard indicators were determined using both AHP and EWM, representing subjective and objective perspectives, respectively. Five experts in the coal-mining field were invited to score the evaluation indicators, and the corresponding judgment matrices were obtained (Table 2-4). The calculation

Indicators	C1	C2
C1	1	1/5.58
C2	5.58	1

Table 3. Judgment matrix for activity indicators.

Indicators	C3	C4
C3	1	1.55
C4	1/1.55	1

Table 4. Judgment matrix for spatiotemporal indicators.

Indicators	Information Entropy	Information Utility Value	ω_{EWM}
Daily frequency of floor MS events	0.9126	0.0874	0.1409
Daily frequency of MS events in the Benxi Formation and deeper strata	0.7944	0.2056	0.3315
Maximum depth of floor MS activity	0.8464	0.1536	0.2476
Advance influence distance of MS events	0.9538	0.0462	0.0745
Daily cumulative energy of floor MS events	0.8725	0.1275	0.2056

Table 5. EWM calculation results.

Indicators	ω_{AHP}	ω_{EWM}	$\omega_{AHP} \times \omega_{EWM}$	ω
Daily frequency of floor MS events	0.0716	0.1409	0.010145	0.049015
Daily frequency of MS events in the Benxi Formation and deeper strata	0.3998	0.3315	0.107738	0.520538
Maximum depth of floor MS activity	0.2478	0.2476	0.023691	0.114464
Advance influence distance of MS events	0.1597	0.0745	0.040111	0.193799
Daily cumulative energy of floor MS events	0.1210	0.2056	0.025289	0.122184

Table 6. Table of weight calculation results.

results of the EWM are shown in Table 5. The composite weights (ω) were then calculated by combining the two methods, as summarized in Table 6.

According to the composite weights, the ranking of the indicators from highest to lowest importance is as follows: daily frequency of MS events in the Benxi Formation and deeper strata > advance influence distance of MS events > daily cumulative energy of floor MS events > maximum development depth of floor MS events > daily frequency of floor MS events.

Comprehensive evaluation of floor water inrush hazard

The floor water inrush hazard evaluation model was established by combining the composite weights of each indicator with their quantitative normalized values as follows:

$$I_i = 0.072280x_{i1} + 0.489597x_{i2} + 0.026968x_{i3} + 0.260178x_{i4} + 0.150976x_{i5}$$

The daily comprehensive hazard index was calculated and compared with the observed water inflow data of the working face, as shown in Figure 16. The comprehensive index was classified into risk levels using equal interval division: low risk (0–0.3), medium risk (0.3–0.6) and high risk (0.6–0.9).

As shown in Figure 16, from April to June, the comprehensive index remained within the low-risk range, consistent with stable water inflow. In late June, some daily indices entered the medium-risk range, accompanied by minor fluctuations in water inflow. From July 1 to 21, the comprehensive index reached the high-risk range, with a peak on July 14, corresponding to the maximum observed water inflow. In August, some indices reached the medium-risk range, while individual indices reached high-risk levels. During this period, water inflow increased significantly, and as the working face entered the “secondary square” stage, mining-induced stress further enhanced floor failure depth, increasing the water inrush hazard. The linear regression between the vulnerability index and the inflow rate is shown in Figure 18. The Pearson correlation coefficient calculated using Equation (9), is 0.682, with an R^2 value of 0.465, indicating a significant correlation.

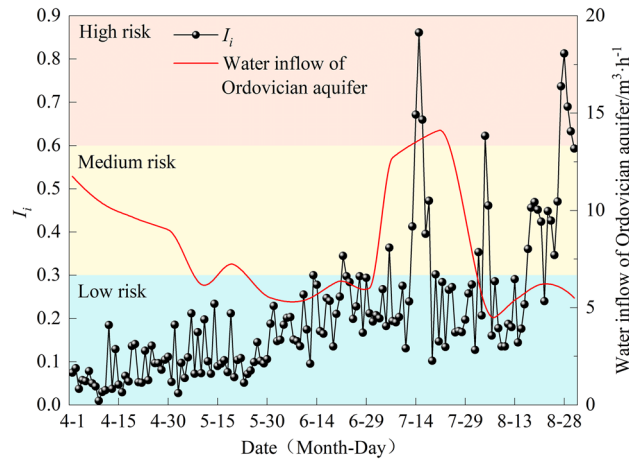


Fig. 16. Comprehensive evaluation of floor water inrush risk.

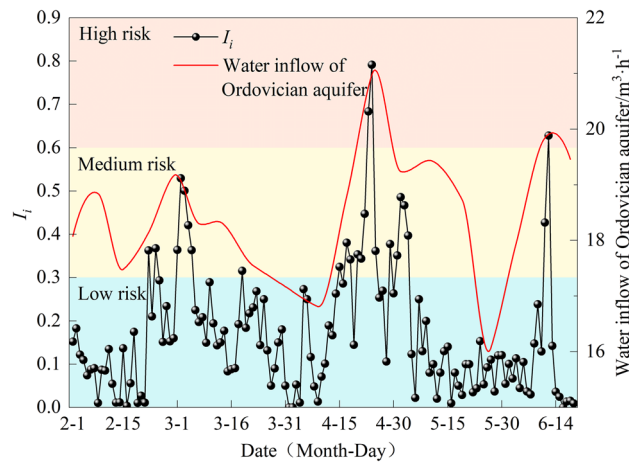


Fig. 17. Verification of the comprehensive evaluation of floor water inrush risk (February–June 2024).

$$r = \frac{\sum_{i=1}^n (x_i - \bar{x})(y_i - \bar{y})}{\sqrt{\sum_{i=1}^n (x_i - \bar{x})^2} \sqrt{\sum_{i=1}^n (y_i - \bar{y})^2}} \tag{9}$$

The evaluation model was further applied to MS events data from February to June 2024 for calculation and validation (Figure 17). The results indicate that the comprehensive floor water-inrush risk index is generally consistent with the variation in inflow rate. The linear regression relationship is shown in Figure 18. The Pearson correlation coefficient is 0.825, with an R^2 value of 0.681, demonstrating a significant correlation. Therefore, the proposed comprehensive evaluation index can be effectively used for water-inrush early warning.

Discussion and outlook

This study takes the Longwanggou Coal Mine in the Zhun’geer Coalfield, China as an example and employs MS monitoring technology to investigate the dynamic evolution characteristics of floor MS events during thick coal seam mining. By analyzing the spatiotemporal response characteristics of floor MS events (time, space, and energy), the correlations between various indicators and floor failure were assessed, and an AHP-EWM-based floor water inrush hazard evaluation model was established, providing guidance for the mining of thick coal seams. In fact, floor fracturing induced by thick coal seam mining results from the dynamic coupling of mining-induced stress, surrounding rock properties, and stratigraphic structure, making it more complex than thin- or medium-thickness coal seam mining. This study provides a preliminary investigation based on MS monitoring results.

- (1) Stress transfer characteristics of floor fracturing.

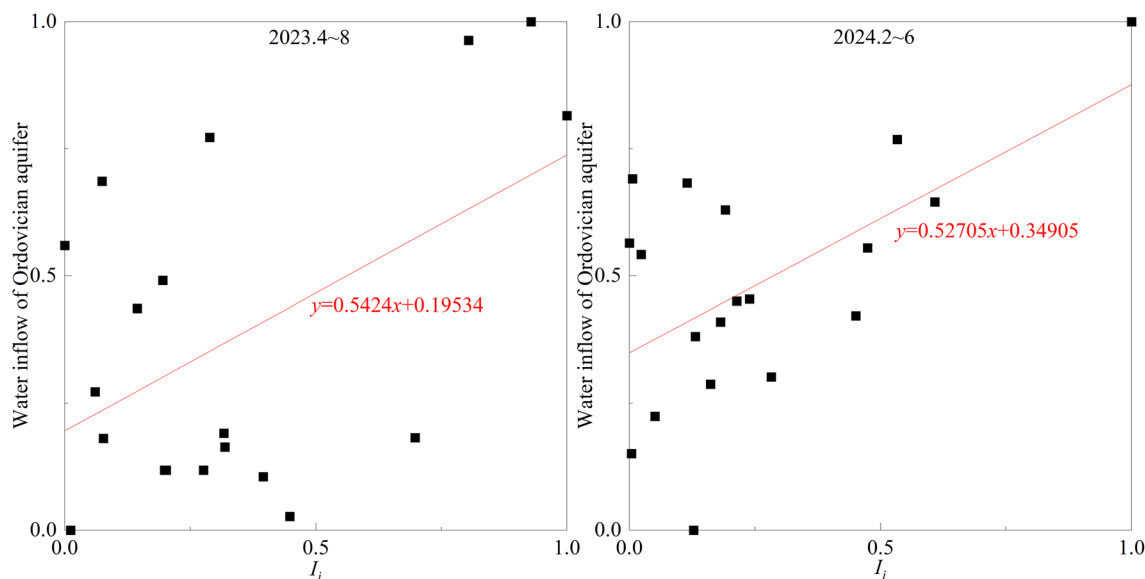


Fig. 18. Linear regression fitting.

In thick coal seam mining, the larger mined-out space significantly increases the depth and intensity of stress transfer to the floor. The maximum concentrated destruction depth of MS events reaches 26.66 m in the middle and lower Taiyuan Formation, and MS events are still detectable in the Benxi Formation and deeper strata (beyond 34.14 m), accounting for ~8% of total events, contrasting with thin- or medium-thickness seams where floor failure is typically within 10 m. This is primarily because thick coal seam mining induces a wider roof movement and more intense stress release, generating energy release in deep floor strata and forming a vertically layered fracture pattern: shallow dense fractures → middle gradual fractures → deep localized fractures. From a water inrush hazard perspective, the floor fracture mechanism directly controls the formation of water-conducting channels. While shallow fractures are dense, they rarely connect to the Ordovician high-pressure aquifer, whereas deep fractures, when combined with aquifer pressure, can trigger a “fracture propagation – hydraulic lift” coupled disaster process. The high correlation between daily frequency of MS events in the Benxi Formation and deeper strata and water inrush risk (subjective weight 0.3998, objective weight 0.3315, composite weight 0.5205) confirms that deep floor fracturing is a key early-warning factor, supporting the shift of mitigation focus to deeper strata.

(2) Dynamic evaluation using MS monitoring

Previous floor water inrush evaluations often relied on static indicators. This study constructs a dynamic indicator system based on MS monitoring, comprising activity, spatiotemporal, and intensity indicators, and applies the AHP-EWM combined weighting method to determine indicator weights. By integrating subjective and objective weights, the reliability and scientific validity of the evaluation are enhanced. The combined weighting results are consistent with field monitoring data, demonstrating the method’s effectiveness.

(3) Limitations and future research directions

The current MS monitoring dataset covers a limited temporal span, excluding the full mining cycle (e.g., initial and periodic stress manifestation stages), which may introduce bias in weight calculations. Moreover, the selected evaluation indicators do not consider multi-factor coupling effects, such as rock mechanical properties or grouting reinforcement coverage, potentially causing deviations between predicted and actual water inrush risk under complex geological conditions.

Future research could focus on:

Extending monitoring duration and expanding the indicator system: Cover the full mining cycle and incorporate factors such as floor rock integrity coefficients and grouting reinforcement effectiveness, constructing a “dynamic MS – static geological – engineering intervention” multidimensional evaluation system to improve comprehensiveness.

Mechanism study with numerical simulation: Develop a floor stress-fracture numerical model for thick coal seam mining, and compare the simulated fracture depth and energy distribution with MS monitoring data to reveal the “mining-induced stress – rock fracturing – hydraulic lift” coupled disaster thresholds, providing a theoretical basis for weight optimization.

Development of intelligent early-warning systems: Based on the AHP-EWM evaluation model and real-time MS monitoring data, develop an integrated system of data acquisition → weight calculation → risk classification → early-warning issuance, enabling dynamic and automated water inrush risk prediction, thereby supporting safe and efficient mining of thick coal seams.

Conclusions

- (1) Based on continuous MS monitoring of the 61607 working face in the Longwanggou Coal Mine, this study systematically characterizes the spatiotemporal response of floor MS activity induced by extremely thick coal-seam mining. The results show that MS events are mainly concentrated within the Taiyuan Formation and exhibit coordinated increases in frequency, depth, spatial extent, and energy release as the working face advances. In combination with observed inflow rates and mine pressure data, MS indicators such as the extent of the advance-affected zone, floor damage depth, and daily cumulative energy show clear responses, revealing the full spatiotemporal evolution of floor failure.
- (2) The characteristics of the recorded MS events indicate that floor microseismicity induced by extremely thick coal-seam mining exhibits the features of “deep occurrence–wide spatial distribution–high energy release.” Deep MS events within the Benxi Formation and underlying strata are strongly associated with aquifer disturbance, structural reactivation, and groundwater movement. These events serve as critical indicators for identifying deep water-related hazards and significantly enhance the accuracy of floor water-inrush early warning.
- (3) By summarizing the key controlling factors of floor water-inrush risk, a dynamic MS indicator system—incorporating event activity, spatiotemporal distribution, and intensity characteristics—was established. Using the AHP–EWM combined weighting method, a quantitative evaluation model for floor water-inrush risk was constructed. The evaluation results show strong consistency with field monitoring data, confirming the applicability and effectiveness of the model under extremely thick coal-seam mining conditions.

Data availability

The authors declare that all data presented in this manuscript are available to researchers for noncommercial use, provided participant confidentiality is maintained. Data requests can be directed to the corresponding author.

Received: 30 October 2025; Accepted: 11 December 2025

Published online: 25 December 2025

References

1. Tian, G., Shang, X., Li, J. & Wang, Y. A strategic study of coal exploitation in Shanxi, Shannxi and Inner Mongolia. *Coal Geol. China* **20**, 1–15 (2008).
2. Zhang, Z. et al. Overburden destruction structure model and mechanism of mine pressure in Caojiatan coal mine with 10 m super large mining height. *J. China Coal Soc.* **50**, 1951–1964 (2025).
3. Pan, C., Xia, B., Zuo, Y., Yu, B. & Ou, C. Mechanism and control technology of strong ground pressure behaviour induced by high-position hard roofs in extra-thick coal seam mining. *Int. J. Min. Sci. Technol.* **32**, 499–511 (2022).
4. Feng, D. et al. Research on overburden structural characteristics and support adaptability in cooperative mining of sectional coal pillar and bottom coal seam. *Sci. Rep.* **14**, 11458 (2024).
5. Lin, H. et al. Study on the energy evolution mechanism and fractal characteristics of coal failure under dynamic loading. *ACS Omega*. **10**, 54710–54719 (2025).
6. Cao, Z. et al. Disaster-causing mechanism of spalling rock burst based on folding catastrophe model in coal mine. *Rock Mech. Rock Eng.* **58**, 7 (2025).
7. Dong, S. et al. Theoretical framework and key technology of advance regional control of water inrush in coal seam floor. *Coal Geol. Explor.* **51**, 185–195 (2023).
8. Yin, S. et al. Mechanism and full-time-space prevention and control technology of water inrush from Ordovician and thin limestone in deep mines. *J. China Coal Soc.* **45** (2020).
9. Zheng, G., Xu, X., He, Y., Ren, C. & Liu, B. Mechanism of Ordovician limestone water inrush from the floor of caving mining face in thick coal seam and water hazard detection technology of nearly horizontal borehole. *Coal Geol. Explor.* **47**, 7–13 (2019).
10. Shao, Q. H. Study on roof and floor failure law of fully mechanized caving mining under the extra-thick coal seam—A case study of Longwanggou Coal Mine. Master's thesis Anhui Univ. Sci. Technol. (2022) (in Chinese)
11. Li, H., Tang, S. B., Kang, Z. Q., Yang, D. & Ma, L. Q. CFDEM simulation on the linkage effect between floor fault failure and roof collapse in ultra-thick coal seam. *J. China Coal Soc.* **49**, 2615–2629 (2024) ((in Chinese)).
12. Wang, S. Study on the evolution law of mining-induced fractures in the floor of extra-thick coal seam fully mechanized top-coal caving mining. Master's thesis Henan Polytech. Univ. (2024) (in Chinese)
13. Li, A. et al. Numerical simulation and experimental study on floor failure mechanism of typical working face in thick coal seam in Chenghe mining area of Weibei. *China. Environ. Earth Sci.* **79**, 118 (2020).
14. He, T., Li, G. D., Sun, C., Luo, F. & Li, X. Q. Floor failure characteristics of thick coal seam mining above confined aquifer. *Min. Metall. Explor.* **39**, 1553–1562 (2022).
15. Zhang, P., Ou, Y., Sun, B. & Liu, C. A case study of floor failure characteristics under fully mechanised caving mining conditions in extra-thick coal seams. *J. Geophys. Eng.* **17**, 813–826 (2020).
16. Liu, C. et al. Comprehensive research on the failure evolution of the floor in upper mining of deep and thick coal seam. *J. Appl. Geophys.* **206**, 104774 (2022).
17. Zhou, W., Zhang, P., Wu, R. & Hu, X. Dynamic monitoring the deformation and failure of extra-thick coal seam floor in deep mining. *J. Appl. Geophys.* **163**, 132–138 (2019).
18. Zhang, P. et al. Comprehensive testing research on floor damage characteristics of mining extra-thick seam in Jungar Coalfield. *Coal Geol. Explor.* **49**, 30 (2021).
19. Guo, G. Floor failure law of extra-thick coal seam in fully mechanized caving mining. *Coal Geol. Explor.* **50**, 13 (2022).
20. Cao, M. et al. Failure mechanism and risk evaluation of water inrush in floor of extra-thick coal seam. *Water* **17** (2025).
21. Zhu, Z. et al. Mechanism and control technology of floor heave in fully mechanized top-coal caving faces of ultra-thick coal seams. *China Saf. Sci. J.* **35**, 73 (2025).
22. Zhang, Z. et al. Characteristics and mechanism of strong dynamic load mine pressure in large mining height full-mechanized caving face with multiple thick and hard roof. *J. China Coal Soc.* **50**, 3369–3387 (2025).
23. Li, J. & Zhao, B. Research on strong mine pressure behavior and control technology in an extra-thick coal seam working face. *Coal Eng.* **57**, 75–81 (2025) ((in Chinese)).
24. Kong, X. et al. Fracture-seepage characteristic zones of the overburden of extra-thick coal seams: evolutionary patterns and their engineering applications. *Coal Geol. Explor.* **53**, 102–113 (2025).

25. Meng, H. L., Cheng, X. G. & Qiao, W. Research on the evolution and prediction of heights of water-conducting fracture zones in overlying rocks during layered mining of extremely thick coal seams. *Ind. Mine Autom.* **50**, 67–75 (2024) ((in Chinese)).
26. Yu, B. et al. Disaster mechanism and collaborative control technology of multi-field coupling in extra-thick coal seam with hard roof. *Coal Sci. Technol.* **53**, 1–16 (2025) ((in Chinese)).
27. Li, N., Wang, E. Y. & Ge, M. C. Microseismic monitoring technique and its applications at coal mines: present status and future prospects. *J. China Coal Soc.* **42**, 83–96 (2017).
28. Yin, H. et al. A deep learning-based data-driven approach for predicting mining water inrush from coal seam floor using microseismic monitoring data. *IEEE Trans. Geosci. Remote Sens.* **61**, 1–15 (2023).
29. Xin, C., Jiang, F., Zhai, C. & Chen, Y. Analysis of coal floor fault activation inducing water inrush using microseismic monitoring—a case study in Zhaogu No. 1 coal mine of Henan Province, China. *Sustainability* **15**, 7361 (2023).
30. Jia, J., Zhou, J. & Niu, Q. Dynamic evolution characteristics and risk assessment of floor microseismic in close repeated mining. *Coal Sci. Technol.* **53**, 46–57 (2025).
31. Huang, L. et al. Research on the development law of pre-mining microseisms and risk assessment of floor water inrush: a case study of the Wutongzhuang coal mine in China. *Sustainability* **14**, 9774 (2022).
32. Gai, Q., Gao, Y., Zhang, X. & He, M. A new method for evaluating floor spatial failure characteristics and water inrush risk based on microseismic monitoring. *Rock Mech. Rock Eng.* **57** (2024).
33. Gai, Q., Gao, Y., Huang, L., Shen, X. & Li, Y. Microseismic response difference and failure analysis of roof and floor strata under dynamic load impact. *Eng. Fail. Anal.* **143**, 106874 (2023).
34. Xu, Y. & Huang, L. Full-time and space early-warning method for floor water inrush in working face based on microseismic monitoring. *Coal Sci. Technol.* **51**, 369–382 (2023).
35. Huang, L. Study on full-time and space prediction and evaluation for floor water inrush at the working face based on microseismic monitoring. Doctoral dissertation China Univ. Mining Technol. (Beijing) (2023) (in Chinese)
36. Zuo, J., Wu, G., Du, J., Lei, B. & Li, Y. Rock strata failure behavior of deep Ordovician limestone aquifer and multi-level control technology of water inrush based on microseismic monitoring and numerical methods. *Rock Mech. Rock Eng.* **55**, 4591–4614 (2022).
37. Ma, K. et al. Floor water inrush analysis based on mechanical failure characters and microseismic monitoring. *Tunn. Undergr. Space Technol.* **108**, 103698 (2021).
38. Liu, R., Zhi, G., Yang, S. & Xu, X. Investigation on mining-induced floor water inrush from column and its control based on microseismic monitoring. *Adv. Civ. Eng.* **2023**, 3754079 (2023).
39. Nie, B. S., Yuan, S. F., Wang, L. K., Zhang, J. L. & Su, X. Q. Roadway roof stability analysis based on microseismic monitoring technology. *Coal Mine Saf.* **47**, 178–180 (2016) ((in Chinese)).
40. Su, Z. Z. Research on the monitoring and early-warning system of mine water in Jining Mine. Master's thesis North China Inst. Sci. Technol. (2021) (in Chinese)
41. Bai, J. J. & Lü, Y. L. Comparative analysis of two kinds of microseismic monitoring systems under collaborative verification mode. *Shandong Coal Sci. Technol.* **11**, 187–189 (2020) ((in Chinese)).
42. Yang, Q. J., Wang, D. P. & He, Q. F. Research and application of microseismic monitoring technology for large dip angle coal seam. *Energy Conserv.* **11**, 160–164 (2022) ((in Chinese)).
43. Chang, J. E. & Jiang, T. L. Research on the weight of coefficient through analytic hierarchy process. *J. Wuhan Univ. Technol.* **29**, 153–166 (2007).
44. Deng, X., Li, J. M., Zeng, H. J., Chen, J. Y. & Zhao, J. F. Analysis and application of weight calculation methods in analytic hierarchy process. *Math. Pract. Theory* **42**, 93–100 (2012) ((in Chinese)).
45. Ishizaka, A. & Labib, A. Review of the main developments in the analytic hierarchy process. *Expert Syst. Appl.* **38**, 14336–14345 (2011).
46. Yang, L., Liu, C. C. & Song, L. Evaluation of coal mine emergency rescue capability based on entropy weight method. *China Soft Sci.* **11**, 185–192 (2013).
47. Zhu, Y., Tian, D. & Yan, F. Effectiveness of entropy weight method in decision-making. *Math. Probl. Eng.* **2020**, 3564835 (2020).
48. Li, J. L. et al. Application and suggestion on vulnerable index method of coal seam floor water burst evaluation. *J. China Coal Soc.* **39**, 725–730 (2014).
49. Wu, Q. & Zhang, S. A new practical methodology of the coal floor water bursting evaluating II—the vulnerable index method. *J. China Coal Soc.* **32**, 1121–1126 (2007).
50. Wu, Q., Liu, Y., Liu, D. & Zhou, W. Prediction of floor water inrush: the application of GIS-based AHP vulnerable index method to Donghuantuo coal mine. *China. Rock Mech. Rock Eng.* **44**, 591–600 (2011).
51. Qiang, W., Li, Y. & Liu, Y. Using the vulnerable index method to assess the likelihood of a water inrush through the floor of a multi-seam coal mine in China. *Mine Water Environ.* **30**, 54–60 (2011).
52. Zeng, Y. et al. Vulnerability assessment of water bursting from Ordovician limestone into coal mines of China. *Environ. Earth Sci.* **75**, 1431 (2016).
53. Meng, H. et al. Mechanism and criterion of water burst in thick plate zone with pressure mining. *China Coal Soc.* **50**(S1), 250–262 (2025) ((in Chinese)).

Acknowledgements

The author gratefully acknowledges the funding and assistance from proof-readers and editors.

Author contributions

Haorui Wang conceived the research and wrote the initial draft of the paper, Shangxian Yin and Huiqing Lian provided guidance for the on-site experiments, Min Cao was responsible for data processing and chart drawing, Enke Hou and Xu Wang proofread and translated the paper, and Guofu Xing provided the experimental site. All authors reviewed, revised, and approved the final version of the manuscript.

Funding

National Key Research and Development Program of China (No. 2022YFC3005905-1); Project under the Central-Guided Fund for Local Science and Technology Development (No. 246Z7604G); Hebei Natural Science Foundation Project (No. D2025508011); The Fundamental Research Funds for the Central Universities (No. 3142025007).

Declarations

Competing interests

The authors declare no competing interests.

Informed consent

All experts involved in the experimental part of this study were fully informed of the research objectives, procedures, and intended use of the collected data. Their participation was entirely voluntary, and each provided explicit informed consent before taking part in the study.

Additional information

Correspondence and requests for materials should be addressed to H.W. or M.C.

Reprints and permissions information is available at www.nature.com/reprints.

Publisher's note Springer Nature remains neutral with regard to jurisdictional claims in published maps and institutional affiliations.

Open Access This article is licensed under a Creative Commons Attribution-NonCommercial-NoDerivatives 4.0 International License, which permits any non-commercial use, sharing, distribution and reproduction in any medium or format, as long as you give appropriate credit to the original author(s) and the source, provide a link to the Creative Commons licence, and indicate if you modified the licensed material. You do not have permission under this licence to share adapted material derived from this article or parts of it. The images or other third party material in this article are included in the article's Creative Commons licence, unless indicated otherwise in a credit line to the material. If material is not included in the article's Creative Commons licence and your intended use is not permitted by statutory regulation or exceeds the permitted use, you will need to obtain permission directly from the copyright holder. To view a copy of this licence, visit <http://creativecommons.org/licenses/by-nc-nd/4.0/>.

© The Author(s) 2025